Nature Communications

https://doi.org/10.1038/s41467-026-73384-7

Article in Press

Electrochemical and chemical cascade catalysis for efficient hexamethylenetetramine synthesis over mesoporous copper nanotips

Received: 4 January 2026

Accepted: 12 May 2026

Cite this article as: Sun, L., Jing, Y., Liu, B. Electrochemical and chemical cascade catalysis for efficient hexamethylenetetramine synthesis over mesoporous copper nanotips. *Nat Commun* (2026). https://doi.org/10.1038/s41467-026-73384-7

Lizhi Sun 孙立智, Yuqian Jing 景雨倩 & Ben Liu 刘犇

Electrochemical and chemical cascade catalysis for efficient hexamethylenetetramine synthesis over mesoporous copper nanotips

Lizhi Sun (孙立智)[1,2+], Yuqian Jing (景雨倩)[1+], and Ben Liu (刘犇)[1*]

[1]Key Laboratory of Green Chemistry and Technology of Ministry of Education, National and Local Joint Engineering Laboratory of Energy Plant Bio-fuel Preparation and Utilization, College of Chemistry, Sichuan University, Chengdu 610064, China. *Corresponding author. *E-mail: ben.liu@scu.edu.cn

[2]Jiangsu Key Laboratory of New Power Batteries, Jiangsu Collaborative Innovation Center of Biomedical Functional Materials, School of Chemistry and Materials Science, Nanjing Normal University, Nanjing 210023, China

[+]These two authors contributed equally to this work.

Abstract: Catalytic carbon-nitrogen (C–N) coupling reactions offer a sustainable and environmentally friendly route for the production of high value-added hexamethylenetetramine (HMTA). However, it still suffers from limited chemisorption, low activation kinetics, and unfavorable thermodynamics, resulting in low HMTA Faradaic efficiency (FE_{HMTA}) and yield rate. Here, by physically constructing hierarchically tip and mesoporous structure, copper mesoporous nanotips (Cu MNTs) realize efficient HMTA synthesis by an electrochemical-chemical cascade catalysis. Unlike traditional catalysts, tip-enhanced site of Cu MNTs electrochemically favors NO_3^- chemisorption and further electroreduction into $*NH_3$ radicals, while its confined mesoporous nanoreactor ensures cascade chemical C–N coupling and subsequent cyclization to HMTA. With minor byproducts, Cu MNTs deliver a FE_{HMTA} of 94.2% and a yield rate of 0.227 mmol h^{-1} cm^{-2}. Moreover, this route enables efficient HMTA synthesis in a flow cell electrolyzer with high economic feasibility and market potential for industrial application. This work thus deepens the physical design strategies of hierarchically structural catalysts that promote electrochemical-chemical cascade C–N coupling reactions for efficient synthesis of various important chemicals and feedstocks.

Introduction

Electrocatalytic conversion of widespread pollution nitrogen sources such as nitrate ion (NO_3^-) into high-value nitrogen-based compounds represents a sustainable and burgeoning frontier in synthetic chemistry, potentially revolutionizing conventional energy-intensive processes.[1-10] While electrocatalytic nitrate reduction reaction (eNO_3RR) to ammonia has been extensively explored for wastewater treatment and alternative ammonia production, it remains energetically costly for subsequent separation and purification of dilute NH_3 in aqueous solution.[11-14] In contrast, *in situ* coupling reaction of electrochemically generated NH_3 species with carbon feedstocks, which bypasses free NH_3 intermediate, offers a more elegant and atom-economic strategy to directly synthesize high value-added C–N coupled products.[15-19] Of various C–N coupled products available, hexamethylenetetramine (HMTA) represents one of the most important crucial industrial chemicals and ensures extensive applications in pharmaceuticals, resins, fuels, and explosives. Recently, some pioneer works have been reported to dirve electrochemical C–N coupling reactions and thus prepare value-added HMTA.[20,21] Despite promising outlook, significant challenges persist in steering selectivity and achieving high yield rate for targeted C–N coupling products because of intricated multistep reactions.[22-26]

In principle, HMTA synthesis from NO_3^- and HCHO involves electrochemical reduction of NO_3^- into $*NH_3$ and subsequent chemical C–N coupling and cyclization with active *CHO intermediates (**Figure 1a**).[20] Notably, there are two fundamental difficulties for electrochemical and chemical (electrochemical-chemical) cascade synthesis of HMTA that should be overcome in designing efficient metal catalysts.[27-29] First, catalysts should enable efficient chemisorption and activation of reactants and accelerate multi-proton coupled electron transfer route.[22,30] Considering significant differences in electronic property and reactivity between NO_3^- and HCHO, especially, it also requires to enhance mass/electron transfers and enlarge local reactants concentrations near metal sites. Meanwhile, energy barrier of electrochemical protonation step should be lowered to overcome the reaction kinetic bottlenecks in initial electroreduction of NO_3^- to NH_3 and subsequent chemical coupling of C–N bonds.[31,32] Second, C–N coupling reactions involve complex condensation and cyclization reactions. Meanwhile, competitive hydrogen evolution reaction (HER) in an aqueous solution also affects reaction activity and product selectivity.[25] Therefore, designed catalysts have to stabilize key intermediates and further transformation pathways and thus synthesize targeted HMTA with minor thermodynamic and kinetic byproducts.[22]

Here, we proposed a physical design strategy by constructing hierarchical tip and mesoporous structure in one catalyst that enabled high activity and selectivity for HMTA synthesis from NO_3^- and HCHO in H_2O. Compared to low-curvature nanoparticles (NPs) with open surface, copper mesoporous nanotips (Cu MNTs) featured concurrent structural synergies of tip-enhanced electric field and mesopore-induced nanoreactor (**Figure 1b**). On the one hand, densely packed tip structure on catalyst surface effectively promoted electrochemical adsorption and activation of reactants and reduced energy barrier of protonation step for $*NH_3$ formation. On the other hand, mesoporous microenvironment functioned as a confined nanoreactor to enrich and stabilize reactive intermediates, which thermodynamically promoted subsequent cascade chemical C–N coupling and cyclization reaction of $*NH_3$ and HCHO. Leveraging these structural synergies, Cu MNTs demonstrated promising performance in HMTA synthesis, including a FE_{HMTA} of 94.2% and a yield rate of 0.227 mmol h^{-1} cm^{-2} as well as cycling stability of reaching 50 cycles. More importantly, the sustainability of this electrocatalytic technology was validated using a flow cell reactor, yielding HMTA with a purity of 80.7% and a recovery rate of 85.1%, demonstrating its potential for real-world application.

Results

Catalyst characterizations and chemisorption properties

Cu MNTs were prepared through a simple two-step route involving the solution-phase synthesis to form uniform CuO NTs assemblies (**Figure S1**) and further *in situ* electrochemical reduction to generate Cu MNTs with penetrated mesopores. During the process, *in situ* electroreduction induced the oxygen removal and atomic reconstruction, which thus produced abundant and highly distributed mesopores while perfectly retaining NT structure. The whole synthesis did not require the utilization of any mesopore-formed templates and thus ensure the surface-clean sites to evaluate structural features of MNTs for catalysis.[33]

Powder X-ray diffraction (XRD) results confirmed the oxide-to-metal electroreduction to form metallic Cu (**Figure S2**). Low-magnification high-angle annular dark-field scanning transmission electron microscopy (HAADF-STEM) and TEM images clearly revealed structural feature of products consisting of densely packed NTs, indicating that tip structure was perfectly retained during electrochemical reduction (**Figures 2a and S3**). High-magnification HAADF-STEM images further showed that there were abundant mesopores within NTs (**Figures 2b and S4**). Mesopores of Cu MNTs were interconnected and penetrated with the diameters in the range of 2-5 nm (**Figure S5**). Moreover, high-resolution HAADF-

STEM images displayed the clear lattice spacing distance of 0.21 nm, corresponding to the (111) plane of face-centered cubic (*fcc*) Cu, further indicating metallic phase of product (**Figure 2c**). Meanwhile, there were abundant coordination-unsaturated, high-index Cu sites along the mesopores and tip structure[34], corresponding to high activity of Cu MNTs. These characterization results definitely validated successful preparation of uniform Cu MNTs with tip structure and interconnected mesopore, which thus provided the material foundation for subsequent electrochemical-chemical cascade synthesis of HMTA.

Theoretical insights were then performed to evaluate the potential promotion mechanism of tip structure and interconnected mesopore for C–N coupling reaction. We first employed finite-element method (FEM) simulations to investigate how these structures modulated local electric fields and key reactive species. Compared to nearly planar nanoparticle surfaces, electric field strength around NTs with higher curvature was enhanced , particularly at the nanotips—a critical factor for the adsorption of certain active species (**Figures 2d and S6**). Notably, the simulations of active hydrogen dynamics revealed that electric field rapidly tended to drive H^+ toward tip surface, suggesting a tendency for higher concentrations and longer residence times near the NT surface (**Figure 2e**). Conversely, H^+ concentrations were markedly lower on particle surfaces with weaker electric fields (**Figure S7**). Additionally, we simulated the concentration distribution of the key intermediate NO_2^-. As shown in **Figure 2f**, abundant interconnected mesopores within MNTs showed a preference for NO_2^- capture , resulting in NO_2^- concentrations inside the mesoporous channels that were nearly seven times higher than near the surface. This concentration enhancement potentially contributed to subsequent electrocatalytic hydrogenation and facilitated effective collisions and directed further cyclization of NH_3 and HCHO. It should be noted that FEM simulations were based on idealized models and did not fully capture the dynamic surface reconstruction, solvation effect, and complex interfacial microenvironment under realistic catalytic conditions. Thus, the results should be interpreted as the theoretical indications of possible trends rather than definitive predictions of experimental outcomes.

Electrocatalytic performance for HMTA synthesis

HMTA synthesis in this work was performed in the supporting electrolyte of 0.10 M KOH containing 0.50 M K_2SO_4 with NO_3^- as the nitrogen source and HCHO as the carbon source, in a standard three-electrode H-type electrolytic cell. Linear sweep voltammetry (LSV) curves, with Cu MNTs as catalyst, were first collected in different electrolytes (**Figure 3a**). Notably, onset reduction potential for eNO_3RR was

significantly more preferable than the values for HCHO reduction and hydrogen evolution reaction (HER), in which the highest current density indicated more thermodynamically favorable eNO_3RR in the same condition. Concurrently, when NO_3^- and HCHO coexisted, current density of C–N coupling reaction slightly decreased, compared to pure eNO_3RR, mostly because of competitive adsorption of HCHO that partially occupied active Cu sites for eNO_3RR.[28] These results clearly highlighted high activity of Cu MNTs for potential HMTA synthesis.

Then, electrocatalytic-chemical cascade C–N coupling reaction was conducted over a wide potential range from −0.8 V to −0.1 V (*vs.* the reversible hydrogen electrode (RHE) hereafter). After 2 h of continuous constant-potential electrocatalysis, targeted product of HMTA was analyzed by the proton nuclear magnetic resonance (^{1}H NMR), while key reaction intermediates of NH_3 and NO_2^- were quantitatively collected by the ultraviolet-visible (UV-Vis) spectroscopy (**Figures S8-S11**). With Cu MNTs as catalyst, FE values of HMTA (FE_{HMTA}) exhibited a characteristic volcano-like trend, achieving the FE_{HMTA} values of >88% across a broad low-potential range from −0.5 V to −0.1 V (**Figures 3b and S12**). Correspondingly, it reached a peak FE_{HMTA} value of 94.2% at −0.4 V with a HMTA yield rate of 0.227 mmol h^{-1} cm^{-2}. At the potentials being more negative than −0.5 V, FE_{HMTA} value slightly declined, likely due to progressively enhanced interference from competitive HER. Further analysis was then conducted on the potential-dependent products distributions (**Figure 3c**). Other products, including NO_2^-, NH_3, and H_2, exhibited very low FE values across the potential range, indicating that Cu MNTs conspicuously promoted the electrochemical-chemical cascade reaction for efficient HMTA synthesis (**Figures S13-S15**). Meanwhile, Cu MNTs achieved the highest selectivity of reaching 84.5% for HMTA synthesis at the optimized potential of −0.4 V, further highlighting that the C–N coupling kinetics outperformed other side reactions (**Figure 3d**). Moreover, the reaction durability of selective HMTA synthesis on Cu MNTs was continuously evaluated for reaching 50 cycles (100 h) at a constant potential of −0.4 V (**Figure 3e**). Strikingly, FE_{HMTA} values remained at a near-steady-state level of 92.7 ± 3.2% throughout the cyclic electrocatalysis, with no significant decay in HMTA selectivity and the catalyst structure remaining stable, evidencing the long-term stability of Cu MNTs for efficient HMTA synthesis in electrochemical-chemical cascade C–N coupling reaction (**Figures S16**).

Electrocatalytic mechanism investigation

Intrinsic performance of Cu MNTs for HMTA synthesis was then analyzed and further compared with its counterpart catalysts by normalizing to its electrochemical surface area (ECSA).[35] Here, three catalysts,

including Cu NTs, Cu mesoporous nanospheres (Cu MNs), and Cu nanoparticles (NPs), were evaluated to reveal tip and mesoporous structural feature of Cu MNTs for HMTA synthesis (**Figures S17-S20**). LSV curves showed that, all four catalysts delivered prominently high onset potentials for C–N coupling reaction related to competitive HER (**Figure 4a**). More importantly, compared to other counterpart catalysts, Cu MNTs exhibited higher current density in all potential range, indicating better intrinsic activity in the C–N coupling reaction. Meanwhile, both Cu MNTs and Cu NTs exhibited strong NO_3^- reduction capabilities, suggesting that tip structure kinetically accelerated eNO_3RR (**Figures S21 and S22**). Then, HMTA yield rates of four catalysts were summarized and compared (**Figure 4b**). As applied potentials being increased, there was a clear decreasing order with Cu MNTs > Cu NTs > Cu MNs > Cu NPs, further indicating that tip structure of Cu MNTs and Cu NTs exerted a dominant role in promoting electrochemical-chemical cascade reaction kinetics.

Structural effect on the reaction kinetics was further evaluated and compared under various electrolyte conditions.[20] As presented in **Figure 4c**, current density of Cu NTs consistently exceeded that of Cu MNs and Cu NPs at identical reduction potentials, highlighting the promotion effect of tip structure to activate reactive species (NO_3^-, HCHO, H_2O) and accelerate reduction kinetics.[36] Meanwhile, adsorption/desorption behavior of reactants and intermediates on active Cu sites significantly influenced electrochemical-chemical reaction kinetic efficiency.[37,38] Open-circuit potential (OCP) tests were then conducted to detect the adsorption response of reactants across different structures (**Figure S23**).[39] After NO_3^- and HCHO being injected, Cu MNTs and Cu NTs exhibited more pronounced OCP decreases than Cu MNs and Cu NPs, reflecting the stronger adsorption capacity of tip structure for NO_3^- and HCHO (**Figure 4d**), attributed to the tip-enhanced enrichment effect.[36,40] Moreover, the strong local electric fields induced by tip structure may form favorable local microenvironments near catalyst surface. As such, considering that eNO_3RR step in HMTA synthesis involved the hydrogenation of active hydrogen (*H) generated from H_2O dissociation, we also conducted cyclic voltammetry (CV) tests to evaluate kinetic performance of *H radical formation (**Figure S24**).[41-43] To be emphasized, Cu MNTs and Cu NTs exhibited noticeably larger surface-adsorbed H* peaks than those of Cu MNs and Cu NPs, indicating that tip structure dramatically promoted the dissociation of interfacial H_2O molecules to form *H. Upon the addition of NO_3^-, H* desorption peak markedly weakened on Cu MNTs surfaces, which was presumably consumed by NO_3^- reduction. It further indicated that tip-enhanced local electric field promoted H* enrichment on Cu surfaces[44,45], which correspondingly increased local concentration and collision frequency with NO_3^-, synergistically accelerating eNO_3RR kinetics. Furthermore, *in situ* electrochemical

impedance spectroscopy (EIS) was employed to validate structural effect on reaction kinetics for HMTA synthesis (**Figure S25**).[20] Evidently, kinetic rate of C–N coupling reaction was considerably faster than that of other reduction reactions (**Figure S26**). Meanwhile, Cu MNTs and Cu NTs with tip-enhanced effect hold faster interfacial reaction charge transfer rates under different electrolyte conditions, further highlighting the crucial role of tip structure in promoting electrochemical-chemical cascade reaction for HMTA synthesis (**Figure S27**).

Promotion mechanism of Cu MNTs for efficient HMTA synthesis from NO_3^- and HCHO was further revealed by comparing FE_{HMTA} values and HMTA selectivity of above four catalysts (**Figures S28 and S29**). Intriguingly, compared to Cu NTs with enhanced enrichment effect, Cu MNs exhibited better performance for HMTA synthesis, indicating that penetrated mesopores played a crucial role to enhance the selectivity of cascade reaction for HMTA synthesis (**Figure 4e,f**). To elucidate why penetrated mesopores in Cu MNTs promoted HMTA synthesis, we then analyzed the formation rates of key intermediates NO_2^- and NH_3. By monitoring NO_2^- concentrations in the cathode electrolyte, we found that more NO_2^- was desorbed significantly on Cu NTs into the electrolyte compared to other counterpart catalysts (**Figure S30**). In comparison, Cu MNTs, which also featured a tip-enhanced effect, demonstrated the lowest NO_2^- yield and FE_{NO2-} (**Figure 4g**). These results sufficiently confirmed that interconnected mesopores within Cu MNTs functioned as a nanoreactor, where strong confinement effect effectively enriched and stabilized reactive intermediates and substantially increased local concentration and residence time near active sites for key intermediates.[46-49] More importantly, generated $*NO_2$ was instantaneously confined within spatially restricted microenvironment of Cu mesopores, thereby enabling the feasibility of regulating deeper electrochemical reduction of $*NO_2$ to $*NH_3$.[50] Similar conclusion was also corroborated by summarizing NH_3 yield and FE_{NH3} (**Figure S31**).

On the basis of above results and analysis, we experimentally separated structural feature of Cu MNTs into tip structure and penetrated mesopore for efficient HMTA synthesis (**Figure 4h**). On one hand, tip structure intrinsically promoted the adsorption and activation of key reactants (such as NO_3^- and HCHO). Meanwhile, Cu sites along tip curvature surface readily generated a strong localized electric field at low overpotentials, which optimized charge distribution and double-layer structure at the reaction interface, accelerating the initial electron transfer step (eNO_3RR) and creating favorable kinetic conditions for subsequent C–N coupling reaction. On the other hand, penetrated mesopores with three-dimensional interconnected channels functioned as a natural nanoreactor, which trapped unstable reaction intermediates within active mesopores by spatial confinement effect, effectively increasing

their local concentration and prolonging residence time.[51,52] The confined environment within Cu mesopores tremendously promoted ordered condensation and cyclization reactions between *CHO and *NH_3 intermediates and precisely guided the electrochemical-chemical cascade pathway toward selective HMTA synthesis from NO_3^- and HCHO.

To further unveil electrochemical-chemical cascade pathway by which Cu MNTs catalyzed selective synthesis of HMTA from NO_3^- and HCHO, *in situ* Fourier transform infrared spectroscopy (FTIR) and Raman spectroscopy were also employed to monitor the dynamic response, especially for key intermediates, during the catalysis. *In situ* FTIR spectra were first recorded over time at the optimized potential of −0.4 V (**Figure 5a**). Compared to Cu MNs and Cu NPs, Cu MNTs and Cu NTs exhibited earlier depletion of NO_3^- (1352 and 1385 cm^{-1})[53], followed by an upward absorption band corresponding to the N–O antisymmetric stretching vibration of *NO_2[54], indicating that tip structure promoted NO_3^- adsorption and initial reduction (NO_3^- → *NO_2). Concurrently, Cu MNTs and Cu MNs showed a stronger upward absorption band at 1155 cm^{-1} corresponded to the N–O stretching vibration of *NO (a key intermediate in the eNO_3RR pathway)[55], presumably because of mesoporous microenvironment effectively prolonging the residence time and increasing the local concentration of the *NO intermediate. Notably, the intensity of the O–H bending vibration peak for adsorbed H_2O on Cu MNs and Cu NPs was weaker than that on Cu MNTs and Cu NTs, clearly indicating that tip structure facilitated the provision of sufficient *H for the hydrogenation reaction of *NO_x.[53,56] Consequently, Cu MNTs and Cu NTs demonstrated a stronger tendency for upward absorption band intensity at 1439 cm^{-1} associated with NH_4^+[57], validating the enhancement effect of tip structure to accelerate electrochemical kinetics of NO_3^--to-NH_3. Moreover, there was absorption band at 1272 cm^{-1}, 1654 cm^{-1} and 1122 cm^{-1}, corresponding to the C–N stretching vibration of HMTA, the C=N stretching vibration of *CH_2=NH, and the C–O stretching vibrations of *$HOCH_2NH_2$, *$N(CH_2OH)_3$, and *$NH(CH_2OH)_2$, respectively (**Figure S32**).[20,58] Meanwhile, the intensity was stronger with reaction time being increased, indicating continuous synthesis of HMTA. Differently, Cu NTs and Cu NPs presented an extra upward absorption band at 1319 cm^{-1}, which may be attributed to the C–N stretching vibrations of CH_3NH_2, $NH(CH_3)_2$, and $N(CH_3)_3$. It confirmed, with mesoporous nanoreactor, that byproducts were more readily formed in weaker confinement microenvironments. Moreover, Cu MNTs and Cu NTs revealed stronger HMTA peaks than Cu MNs and Cu NPs, a result of the tip-enhanced effect accelerating catalytic kinetics of C–N coupling reaction.

To further validate proposed mechanism, *in situ* Raman spectroscopy of Cu MNTs was employed and further compared with Cu NPs to monitor the C–N coupling process at different potentials (**Figures**

5b,c). There were only five characteristic peaks at OCP, which corresponded to SO_4^{2-} (979 cm^{-1}), NO_3^- (1047 cm^{-1}), HCHO (1494 cm^{-1}), and carbon paper (1314 and 1594 cm^{-1}) (**Figure S33**). As the applied potential being increased, peak intensities of $\nu_s NO_3^-$ and δH-C-H on Cu NPs gradually decreased, indicating continuous depletion of NO_3^- and HCHO. However, sustained strong adsorption of reactants on Cu MNTs, coupled with a rapid reduction mechanism, retained peak intensity without significant decay. Concurrently, there were a series of new peaks appeared on Cu MNTs, which corresponded to key nitrogen/carbon intermediates and products. Compared to Cu NPs, Cu MNTs disclosed more pronounced peak intensities, further indicating its accelerated C–N coupling rate for HMTA synthesis. More notably, there were two characteristic ν_sNCN and τCH_2 peaks at near 1016 and 1349 cm^{-1}, providing strong evidence for directed coupling between *HCHO and $*NH_3$ to form HMTA.[30,31,59-61]

From above analysis, we reasonably proposed an electrochemical-chemical cascade pathway for HMTA synthesis from NO_3^- and HCHO over Cu MNTs (**Figures 5d**). The initial step involved electrochemical eNO_3RR on tip structure of MNTs, which relied on tip-enhanced effect to convert a large amount of NO_3^- adsorbed on Cu MNTs into $*NO_2$. Subsequently, within confined nanoreactor of mesoporous microenvironment, $*NO_2$ was electrochemically reduced to *NO and $*NH_3$ in sequence. After that, a series of cascade chemical reactions further occurred within active mesoporous nanoreactor. Formed $*NH_3$ combined with *HCHO to generate $*HOCH_2NH_2$ intermediate and further lose H_2O to form $*CH_2$=NH.[20] Meanwhile, $*HOCH_2NH_2$ continuously reacted with *HCHO to sequentially form $*N(CH_2OH)_3$ and $*NH(CH_2OH)_2$. Moreover, confined mesoporous nanoreactor ensured orientations on the conformation of reaction intermediates and reaction pathways. In addition to rapid mass and electron transport, electrochemical-chemical cascade pathway of Cu MNTs thus delivered high efficiency and stability for HMTA synthesis over linear byproducts such as CH_3NH_2, $NH(CH_3)_2$ and $N(CH_3)_3$.

Product purification and economic analysis

Beyond the high performance of Cu MNTs in standard H-type electrolytic cell, flow cell was also of critical importance for practical synthesis of HMTA from NO_3^- and HCHO. Here, we assembled a three-electrode flow cell for HMTA synthesis to validate practical feasibility of Cu MNTs catalyst (**Figure 6a**). As shown in **Figures 6b,c**, this system achieved favorable HMTA production efficiency, with FE_{HMTA} value of 92.2% and HMTA selectivity of 82.4% as well as HMTA yield rate of 0.53 mmol h^{-1} cm^{-2} at −0.4 V. Meanwhile, there was a promising stability, even for cascade catalysis for 60 h constant-potential test at −0.4 V, which retained high FE_{HMTA} value and HMTA yield rate (**Figure 6d**). High HMTA yield rate and FE_{HMTA}

value significantly simplified downstream HMTA purification processes and reduce costs. Consequently, after reaction completion, the electrolyte underwent further acidification, evaporation crystallization, and vacuum filtration to ultimately isolate high-purity HMTA (**Figures 6e and S34-S36**). The ^{1}H NMR analysis confirmed the recovery of approximately 1.14 g of HMTA, with a purity and recovery rate of 80.7% and 85.1%, respectively. Meanwhile, based on actual processing efficiency estimates, each ton of HMTA produced during flow cell additionally yielded 9840 kg of K_2SO_4, and 442 kg of KNO_3, fully demonstrating broad practical prospects of this technology. More importantly, preliminary technical-economic analysis (TEA) indicated that the profit margin for synthesizing 1 ton of HMTA using this system was approximately $823.2 (see the Supplementary Note 1 for calculation details), which further hold significant importance for advancing green production of HMTA with designed Cu MNT catalyst in industry (**Figure S37**).

Discussion

By constructing concurrent tip and mesoporous structure, we proposed a high-performance Cu MNT catalyst that promoted electrochemical-chemical cascade catalysis for efficient HMTA synthesis from NO_3^- and HCHO. Experiment and mechanism studies revealed that tip-enhanced effect favored reactant adsorption and further accelerated cascade reaction kinetics, while mesoporous nanoreactor stabilized reaction intermediates, facilitating efficient collisions and directed assembly between *CHO and *NH_3 within confined mesopores. This ultimately significantly promoted preferential formation of cyclic HMTA with minor byproducts. Compared with other catalysts with different structures, Cu MNTs afforded a favorable performance for HMTA synthesis, including FE_{HMTA} value of 94.2% and HMTA yield rate of 0.227 mmol h^{-1} cm^{-2} as well as stability of reaching 50 cycles. Moreover, Cu MNTs held high reaction performance in a three-electrode flow cell, enabling robust HMTA production with a high recovery rate of 85.1% and a proper profit margin of approximately $823.2 ton^{-1}. The findings in designing hierarchical structure catalysts offer some opportunity to promote electrochemical-chemical cascade catalysis for robust synthesis of various high-value-added chemicals and products from biomass and environmental wastes.

Methods

Materials and Chemicals

Copper(II) nitrate trihydrate ($Cu(NO_3)_2{\cdot}3H_2O$, 99.9%), copper sulfate ($CuSO_4$, ≥99%), sodium nitroferricyanide dihydrate ($C_5FeN_6Na_2O{\cdot}2H_2O$, 99.0%), sodium hypochlorite (NaClO, 6-14%, active chlorine), salicylic acid ($C_7H_6O_3$, ≥99.5%), hexamethylenetetramine ($C_6H_{12}N_4$), phosphoric acid (H_3PO_4, ≥85 wt.% in H_2O), potassium chloride (KCl, 99.5%), sodium borohydride ($NaBH_4$, ≥98.0%), potassium sulfate (K_2SO_4, 98.5%), and ammonium chloride (NH_4Cl, 99.5%) were purchased from Aladdin. Nafion solution (5 wt% in alcohol and H_2O), N-(1-naphthyl) ethylenediamine dihydrochloride ($C_{12}H_{16}Cl_2N_2$, 98%), and L-ascorbic acid (AA, ≥99%) were obtained from Alfa Aesar. Sulfanilamide ($C_6H_8N_2O_2S$, ≥99%) was purchased from Sigma-Aldrich. Potassium nitrate (KNO_3, 99.0%), potassium nitrite (KNO_2, 99.0%), trisodium citrate anhydrous ($C_6H_5Na_3O_7$, 98%), sulfamic acid (99.5%), p-Dimethylaminobenzaldehyde ($C_9H_{11}NO$, ≥97.0%), hydrochloric acid (HCl, 36.0%-38.0%), formaldehyde (HCHO, 37.0-40.0%), ethanol (C_2H_6O, ≥99.7%), sodium hydroxide (NaOH, ≥96.0%), and potassium hydroxide (KOH, ≥85.0%) were obtained from Sinopharm Chemical Reagent Co. Ltd. (Shanghai). All the reagents are of analytical reagent grade and used without further purification. Deionized H_2O with the resistivity of 18.25 mΩ was used in all experiments.

Synthesis of Cu MNTs and counterpart samples

Synthesis of Cu MNTs. Cu MNTs were prepared *via* a simple two-step process. First, CuO product was obtained through a solution-phase method as followed: 4.0 mL of 10 mM $Cu(NO_3)_2$ was first dispersed in 50 mL of deionized water. Then, 5.0 mL of freshly prepared 0.13 M $NaBH_4$ was rapidly injected into above solution under gentle shaking. After being reacted at room temperature (25 ± 2 ^{O}C) for over 12 h, CuO NTs was collected by being gently centrifugated and washed several times with ethanol/water. The second step involved preparing Cu MNTs *via* in situ electrochemical reduction. Specifically, CuO NTs was fabricated into a working electrode. In 1.0 M KOH, CuO electrode was electrocatalyzed at −1.6 V (vs. Ag/AgCl) for 0.5 h to produce Cu MNTs.

Synthesis of Cu NTs. Cu NTs were synthesized *via* a simple two-step process comprising hydrothermal synthesis and electrochemical reduction. The hydrothermal pre-synthesis of CuO nanoneedles was followed by a route reported by Dar et al.[62] Subsequent electrochemical reduction was consistent with that employed for Cu MNTs.

Synthesis of Cu MNs. Cu MNs were synthesized *via* a simple two-step process comprising solution-phase synthesis and electrochemical reduction. Cu_2O mesoporous spheres were prepared according to

previously reported routes by Liu et al.[63] Subsequent electrochemical reduction was consistent with that employed for Cu MNTs.

Synthesis of Cu NPs. Cu NPs were synthesized *via* a simple two-step process comprising solution-phase synthesis and electrochemical reduction. In a typical synthesis, 1.0 mL of 1.2 M $CuSO_4$ was rapidly injected into 400 mL of deionized H_2O at 25 ^{O}C. After being stirred for 5 min, 1.0 mL of 4.8 M NaOH was injected into the solution. The clear blue solution was immediately turned turbid blue, indicating the formation of $Cu(OH)_2$. After another 5 min, 1.0 mL of freshly prepared AA (1.2 M) was injected and maintained for another 0.5 h. The color of the solution was rapidly turned form turbid blue to yellowish brown. After being centrifugated and decantated with ultrapure water and absolute ethanol for several times, resulting Cu_2O precipitate was performed, followed by being dried in vacuum at room temperature (25 ± 2 ^{O}C) for 12 h. The subsequent electrochemical reduction was consistent with that employed for Cu MNTs synthesis.

Electrochemical measurements

All electrochemical measurements were carried out using a CHI 660E electrochemical workstation (Chenhua, Shanghai) in an H-type electrolytic cell separated by a Nifion 117 membrane (DuPont) with a test temperature of 25 ± 2 ^{O}C. Before the tests, the Nifion 117 membrane was sequentially boiled in 3.0 % H_2O_2 for 1 h and deionized H_2O for 2 h and 0.50 M H_2SO_4 for 1 h. After that, the Nifion 117 membrane was rinsed in deionized H_2O for several times. The electrocatalysts inks were prepared by mixing 10.0 mg of electrocatalysts with a mixed solution of 0.40 mL of ultrapure water, 0.52 mL of ethanol, and 80 μL of Nafion. After being sonicated thoroughly, 100 mL of electrocatalyst ink was dropped onto 0.50 cm^{-2} of carbon paper (catalyst loading amount: ca. 2.0 mg cm^{-2}), followed by natural drying within a culture dish with a cover. A compact film was formed and used as the working electrode in the following electrocatalysis process.

Most of electrochemical experiments were performed using a three-electrode system, in which Ag/AgCl (with saturated KCl as the filling solution) and platinum mesh were used as the reference and counter electrodes, respectively. Ag/AgCl reference electrode was periodically calibrated using the dual-electrode comparison method. Specifically, the potential of the working Ag/AgCl electrode was verified by immersing it in a saturated KCl solution and comparing it with a calibrated standard Ag/AgCl electrode. The potential difference was measured using a multimeter set to the millivolt (mV) range. If the potential deviation remained within ±10 mV, the electrode was considered reliable. During the experiment, the

condition of the internal electrolyte was closely monitored, followed by promote addition of fresh 3.5 M KCl to ensure electrochemical stability and measurement repeatability. The electrolyte solution was prepared fresh as needed. To ensure concentration accuracy, the solution was prepared in a volumetric flask. KOH (85.0% purity), K_2SO_4 (98.5% purity), KNO_3 (99.0% purity), and HCHO (37.0–40.0 wt%) were mixed in deionized water to form the cathode electrolyte (0.10 M KOH + 0.50 M K_2SO_4 + 0.30 M HCHO + 0.10 M KNO_3, pH = 13 ± 0.2). The pH value of the solution was measured using a pH meter. Since electrochemical experiments were conducted in a strongly alkaline environment, the pH at the cathode remained stable within the alkaline range throughout the reaction. On the anode side, although OH^- was consumed, the relatively short duration of each electrochemical measurement prevented significant pH fluctuations. The cathode cell (30 mL, 0.10 M KOH + 0.50 M K_2SO_4 + 0.30 M HCHO + 0.10 M KNO_3) and anode cell (30 mL, 0.10 M KOH) were separated by a Nifion 117 membrane. Electrode potentials were converted to the reversible hydrogen electrode (RHE) reference using $E_{RHE} = E_{Ag/AgCl} + 0.197\ V + 0.0591(pH)$. Before electrocatalytic tests, linear sweep voltammetry (LSV) curves were performed until that the polarization curves achieved the steady-state ones at a rate of 10 mV s^{-1}. Then, the potentiostatic tests were carried out at different potentials for 2.0 h with a stirring rate of 300 rpm. Cyclic voltammetry (CV) curves in electrochemical double-layer capacitance (C_{dl}) determinations were measured in a potential window nearly without the Faradaic process at different scan rates of 40, 60, 80, 100, 120, 140, and 160 mV s^{-1}. In-situ electrochemical impedance spectroscopy (EIS) tests were carried out with frequency range from 1.0 M Hz to 0.10 Hz with AC amplitude of 5.0 mV. All the electrochemical performance tests were without *iR* compensation.

^{1}H NMR spectroscopy

After the electroreduction, the electrolyte was taken out for further quantification by ^{1}H NMR (400 MHz) with external standards of maleic acid. The calibration curves were created as followed: (1) a series of solutions with the known concentrations were prepared as the standards; (2) 0.50 mL of standard solution with different concentrations was mixed with 20 mg of maleic acid; (3) 50 µL of deuterium oxide (D_2O) was added in 0.50 mL of above mixed solution for ^{1}H NMR detection; (4) the calibration was achieved using the peak area ratio between test sample and maleic acid because the sample concentration and the area ratio were positively correlated.

Determination of products

Determination of HMTA: After the electrolytic reaction concludes, remove the electrolyte from the cathode chamber and perform quantitative analysis of the HMTA product using ^{1}H NMR coupled with the maleic acid external standard method. Prior to the analysis, establish a calibration curve following these steps: (1) Prepare a series of HMTA standard solutions with the known concentrations (5, 10, 20, and 30 mmol L^{-1}); (2) Mix 0.50 mL of each standard solution with 20 mg of maleic acid thoroughly; (3) Add 50 μL of D_2O to each mixture for ^{1}H NMR detection; (4) Since sample concentration correlates positively with peak area, the calibration was performed using the ratio of sample to maleic acid peak areas. Under the experimental conditions employed in this work, the chemical shift of the HMTA product peak ranged from 4.61 to 4.64 ppm.

Determination of ammonia: The amounts of NH_3 produced in the reaction solution were determined by colorimetry using the indophenol blue method. Specifically, 2.0 mL of the electrolyte was taken from the reaction cell and further mixed with 2.0 ml of 1.0 M NaOH that contained salicylic acid and sodium citrate. Then, 1.0 mL of 0.05 M sodium hypochlorite and 0.20 ml of 1.0 wt % sodium nitroferricyanide dihydrate were added to the above solution. After standing at room temperature (25 ± 2 °C) for 2 h, the UV-Vis absorption spectroscopy was measured. The concentrations of NH_3 produced were determined using the absorbance at a wavelength of 655 nm.

Determination of nitrate: First, a certain amount of electrolyte was taken out from the electrolytic cell and diluted to 5.0 mL. Then, 0.10 mL of 1.0 M HCl and 0.01 mL of 0.80 wt% sulfamic acid were added into above solution. After standing at room temperature (25 ± 2 °C) for 2 h, the UV-Vis absorption spectroscopy was measured. The concentrations of nitrate were recorded with the absorption intensities at wavelength of 220 nm and 275 nm. The final absorbance value was calculated by the equation as followed: $A=A_{220nm}-2A_{275nm}$.

Determination of nitrite: A mixture containing 4.0 g of p-aminobenzenesulfonamide, 0.20 g of N-(1-naphthyl) ethylenediamine dihydrochloride, 50 mL of ultrapure water, and 10 mL of phosphoric acid (ρ=1.70 g/mL) was used as a color reagent. A certain amount of electrolyte was taken out from the electrolytic cell and diluted to 5.0 mL. Next, 0.10 mL of color reagent was added and mixed uniformly. The absorption intensity was recorded after sitting for 20 min.

Calculation of the yield rate and the Faradaic efficiency of HMTA (FE_{HMTA})

$$4NO_3^- + 6HCHO + 18H_2O + 32e^- \rightarrow C_6H_{12}N_4\ (HMTA) + 36OH^-$$

The yield rate of HMTA can be calculated using the following equation (**Equation 1**):

$$\text{Yield rate (HMTA)} = C_{HMTA} \times V) / (t \times m) \quad (1)$$

The FE_{HMTA} was the percentage of the charge consumed for HMTA generation in the total charge passed through the electrode according to the following equation (**Equation 2**):

$$FE_{HMTA} = (32 \times F \times C_{HMTA} \times V \times 10^{-6}) / Q \times 100\% \quad (2)$$

where C_{HMTA} is the measured HMTA concentration (mmol L^{-1}); V is the volume of the electrolyte (30 mL); t is the electrolysis time (2 h); F is the faraday constant (96485 C mol^{-1}); Q (C) is the total charge passed through the electrode, which is the integral of *i-t* curve. The yield rate, the FE_{HMTA}, and corresponding error bars were obtained from above five individual samples under the same testing conditions.

Calculation of yield rate and Faradaic efficiency of NH_3 (FE_{NH3})

The yield of NH_3 can be calculated using the following equation (**Equation 3**):

$$\text{Yield } (NH_3) = C_{NH3} \times V \quad (3)$$

FE_{NH3} was the percentage of the charge consumed for NH_3 generation in the total charge passed through the electrode according to the following equation (**Equation 4**):

$$FE_{NH3} = (8 \times F \times C_{NH3} \times V \times 10^{-6}) / Q \times 100\% \quad (4)$$

where C_{NH3} is the measured NH_3 concentration (mmol L^{-1}); V is the volume of the electrolyte (30 mL); t is the electrolysis time (2 h); F is the faraday constant (96485 C mol^{-1}); Q (C) is the total charge passed through the electrode, which is the integral of *i-t* curve. The yield rate, the FE_{NH3}, and corresponding error bars were obtained from above five individual samples under the same testing conditions.

Calculation of the Faradaic efficiency of NO_2^- (FE_{NO2-})

The Faradaic efficiency of NO_2^- (FE_{NO2-}) was the percentage of the charge consumed for NO_2^- generation in the total charge passed through the electrode according to the following equation (**Equation 5**):

$$FE_{NO2-} = (2 \times F \times C_{NO2-} \times V \times 10^{-6}) / Q \times 100\% \quad (5)$$

where C_{NO2-} is the measured NO_2^- concentration (mmol L^{-1}); V is the volume of the electrolyte (30 mL); t is the electrolysis time (2 h); F is the faraday constant (96485 C mol^{-1}); Q (C) is the total charge passed through the electrode, which is the integral of *i-t* curve.

Calculation of the Faradaic efficiency of H_2 (FE_{H2})

The amount of H_2 evolved (n_{H_2}) was monitored by gas chromatography (GC) with thermal conductivity detectors (TCD), using CH_4 as the internal standard. The Faradaic efficiency for H_2 evolution was calculated by:

$$FE_{H_2} = \frac{2 \times n_{H_2} \times F}{Q} \times 100\% \quad (6)$$

where F = 96485 C mol^{-1} is the Faradaic constant, n is the molar amount of formed H_2, and Q is the charge passed during electrolysis.

***In Situ* Raman Spectroscopy**

Raman measurements were carried out with 532 nm of excitation by using a confocal Raman microspectrometer (Renishaw, inVia-Reflex, 532 nm). *In situ* Raman measurements were carried out jointly by the aforementioned Raman microscope and a CHI 660 electrochemical workstation. A homemade Teflon cell with a quartz window was used as reactor to enable *in situ* measurements. The cell was equipped with a reference electrode (Ag/AgCl), a counter electrode (Pt ring), and a working electrode with the catalyst drop-casted on carbon paper. The working electrode was immersed into the electrolyte and kept the electrode plane perpendicular to the laser. *In situ* Raman spectra were obtained when the electrodes were under potentiostatic control. The experiment is controlled within 300 s under each fixed potential.

***In situ* FTIR measurements**

In situ FTIR measurements were carried on the Thermo Scientific Nicolet iS50 FTIR SPECTROMETER equipment. The measurements were carried jointly out by aforementioned equipment and a CHI 660E electrochemical workstation. Electrochemical tests were conducted using a three-electrode system, in which a polished Au film, a platinum sheet and an Ag/AgCl (with saturated KCl as the filling solution) were used as the working electrode, counter electrode, and reference electrode, respectively.

Characterizations

TEM and STEM studies were carried out using a field emission TEM (JEM-F200, JEOL Ltd., Japan) with an accelerating voltage of 200 kV. TEM and STEM samples were prepared by dropcasting a diluted suspension of the sample powder onto a carbon coated nickel grid (400 mesh). Notes: Donot using

carbon coated copper grid for TEM characterizations. Powder X-ray Diffraction (PXRD) patterns of powder samples were recorded using a D/max 2500 VL/PC diffractometer (Japan) equipped with graphite-monochromatized Cu Kα radiation in 2ϑ ranging from 30° to 80°. The working voltage and current were 40 kV and 100 mA, respectively.

Finite-element method (FEM) simulations

This simulation employs COMSOL for multiphysics coupling analysis, utilizing electrostatic and rarefied fluid transport.

Ion concentration distribution is simulated using the Nernst-Planck equation and Fick's laws. The Nernst-Planck equation is as follows:

$$J_i = D_i \left(\nabla c_i + \frac{z_i F c_i}{RT} \nabla \varphi \right) + c_i u \quad (7)$$

J is the current density, D_i is the diffusion coefficient, ∇c_i is the concentration gradient, z_i is the charge density, F is Faraday's constant (96485.34 C/mol), R is the gas constant (8.3145 J/(mol·K)), $\nabla \varphi$ is the potential gradient, and u is the velocity. When fluid flow is neglected, u = 0.

Fick's Second Law describes the diffusion of substances due to concentration gradients, with the relevant equation as follows:

$$\frac{\partial C}{\partial t} = \nabla \cdot (D \nabla C) \quad (8)$$

where C is the concentration, t is time, D is the diffusion coefficient, and ∇ is the gradient operator.

Material Parameters: Set the initial hydrogen ion concentration to $1e^{-13}$ mol/m³, NO_2^- to 0 mol/m³, NO_2^- with a constant generation rate of $1e^{-4}$ mol/(m²·s), and diffusion coefficients uniformly set to $1e^{-9}$ m²/s.

Boundary Conditions and Loads: The upper boundary is set as a grounded boundary condition, while the lower boundary is set to a constant potential of -0.4 V.

Data availability

Source data are provided with this paper.

References

1. Chen, S. *et al.* Engineering Cu/Ru Heterointerface-Shelled Nanocavities by the Kirkendall Effect for Highly Efficient Nitrate Electroreduction to Ammonia. *J. Am. Chem. Soc.* **147**, 36494-36507 (2025).
2. Xue, C. *et al.* Electrosynthesis of Nitriles from Nitrate and Aldehyde via C–N Bond Construction. *J. Am. Chem. Soc.* **147**, 32896-32903 (2025).
3. Guan, M.-H. *et al.* Cathode–Anode Synergy Electrosynthesis of Propanamide via a Bipolar C–N Coupling Reaction. *J. Am. Chem. Soc.* **147**, 16301-16308 (2025).
4. Wang, Y. *et al.* Electron Deficiency is More Important than Conductivity in C–N Coupling for Electrocatalytic Urea Synthesis. *Angew. Chem. Int. Ed.* **63**, e202410938 (2024).
5. Han, S. *et al.* Synthesis of liquid nitrogenous fertilizer via a nitrogen conversion balance. *Nat. Sustain.* **8**, 1068-1076 (2025).
6. Wu, J. *et al.* Integrated Tandem Electrochemical-chemical-electrochemical Coupling of Biomass and Nitrate to Sustainable Alanine. *Angew. Chem. Int. Ed.* **62**, e202311196 (2023).
7. Tang, Y. *et al.* Selective electrosynthesis of hydroxylamine from aqueous nitrate/nitrite by suppressing further reduction. *Nat. Commun.* **15**, 9800 (2024).
8. Wang, Y. *et al.* Atomic coordination environment engineering of bimetallic alloy nanostructures for efficient ammonia electrosynthesis from nitrate. *Proc. Natl. Acad. Sci. U.S.A.* **120**, e2306461120 (2023).
9. Zhou, J. *et al.* Constructing molecule-metal relay catalysis over heterophase metallene for high-performance rechargeable zinc-nitrate/ethanol batteries. *Proc. Natl. Acad. Sci. U.S.A.* **120**, e2311149120 (2023).
10. Wu, L. *et al.* Intermittent electrolysis enabling enhanced efficiency and stability for nitrate reduction. *Chem* **11,** 102591 (2025).
11. Wang, P. *et al.* Photothermal-electrocatalysis interface for fuel-cell grade ammonia harvesting from the environment. *Nat. Commun.* **16**, 5581 (2025).
12. Simonov, A. N., Koper, M. T. M. & MacFarlane, D. R. Practical prospects of electroreduction of dilute NO_x streams to ammonia. *Nat. Chem. Eng.* **2**, 398-401 (2025).
13. Ma, Y. *et al.* Unconventional phase metal heteronanostructures with tunable exposed interface for efficient tandem nitrate electroreduction to ammonia. *Nat. Commun.* **16**, 7632 (2025).
14. Li, Q., Li, Y., Xu, B., Yang, J. & Wang, Y. Gram-Scale Ammonia Synthesis via Electrochemical Nitrate Reduction Using Enzyme-Inspired Dual-Atomic Cu Catalyst. *Angew. Chem. Int. Ed.* **64**, e202510139 (2025).
15. Zhang, Y. *et al.* Oxy-reductive C-N bond formation via pulsed electrolysis. *Nat. Commun.* **16**, 8106 (2025).
16. Liu, Y., Sun, Y., Deng, Y. & Qiu, Y. Electrochemical Amination of Aryl Halides with NH_3. *Angew. Chem. Int. Ed.* **64**, e202504459 (2025).
17. Song, Q. *et al.* Electrochemical Oxidation of Methane to Methylamine. *J. Am. Chem. Soc.* **147**, 14966-14971 (2025).
18. Lu, Y. *et al.* Anodic Electrosynthesis of Amide from Alcohol and Ammonia. *CCS Chem.* **6**, 125-136 (2023).
19. Qian, Q. *et al.* Dual-site cooperation for synergistic optimization of the band structure and spin state to facilitate C–N coupling reaction. *Proc. Natl. Acad. Sci. U.S.A.* **122**, e2508077122 (2025).
20. Pan, Y. *et al.* Electrocatalytic Coupling of Nitrate and Formaldehyde for Hexamethylenetetramine Synthesis via C–N Bond Construction and Ring Formation. *J. Am. Chem. Soc.* **146**, 19572-19579 (2024).
21. Li, S. *et al.* Carbon defects enhanced TEMPO redox cycles for high-efficiency urotropine electrosynthesis. *Nat. Commun.* **16**, 10578 (2025).
22. Xu, M. *et al.* Electrocatalytic and Photocatalytic C–N Coupling From Small Molecules. *Adv. Mater.* **38**, 2507144 (2025).
23. Wan, Y., Zheng, M., Yan, W., Zhang, J. & Lv, R. Fundamentals and Rational Design of Heterogeneous C-N Coupling Electrocatalysts for Urea Synthesis at Ambient Conditions. *Adv. Energy Mater.* **14**, 2303588 (2024).
24. Anastasiadou, D. & Costa Figueiredo, M. Electrocatalytic Pathways to the Formation of C–N Bonds. *ACS Catal.* **14**, 5088-5097 (2024).
25. Bai, W. *et al.* Emerging Atomistic Modeling Catalysts for C–N Electrocatalysis. *Adv. Mater.* **38**, e10907 (2026).
26. Chen, X. *et al.* Efficient C–N coupling in the direct synthesis of urea from CO_2 and N_2 by amorphous $Sb_xBi_{1-x}O_y$ clusters. *Proc. Natl. Acad. Sci. U.S.A.* **120**, e2306841120 (2023).
27. Tan, J. *et al.* Dual Active Sites on Cu/Cu_2O Heterostructures for the Cascade Electrocatalytic Synthesis of Amino Acids. *J. Am. Chem. Soc.* **147**, 23635-23642 (2025).
28. Lu, X. *et al.* Multiple Secondary Bond-Mediated C–N Coupling over N-Doped Carbon Electrocatalysts. *J. Am. Chem. Soc.* **147**, 19342-19352 (2025).
29. Wang, H. *et al.* Imidazolium radical-mediated electron transfer enhances electrochemical C–N coupling for glycine synthesis. *Nat. Synth.* **5**, 74-83 (2026).
30. Wang, Y. *et al.* Balancing Intermediates Formation on Atomically Pd-Bridged Cu/Cu_2O Interfaces for Kinetics-Matching Electrocatalytic C–N Coupling Reaction. *Angew. Chem. Int. Ed.* **64**, e202503011 (2025).

31. Zhao, C. *et al.* Tailoring Activation Intermediates of CO_2 Initiates C–N Coupling for Highly Selective Urea Electrosynthesis. *J. Am. Chem. Soc.* **147**, 8871-8880 (2025).
32. Wang, Y. *et al.* Regulating Active Hydrogen Supply Over Cu Clusters-Interspersed MoS_2/MoO_2 Nanosheets for Efficient Urea Electrosynthesis. *Adv. Funct. Mater.* **36**, e19152 (2026).
33. Liu, Y., Fan, D. & Liu, B. Strategies for Template-Free Synthesis of Mesoporous Metal Catalysts with Surface-Clean Sites. *Acc. Mater. Res.* **6**, 1246-1255 (2025).
34. He, M., Li, R., Cheng, C., Liu, C. & Zhang, B. Microenvironment regulation breaks the Faradaic efficiency-current density trade-off for electrocatalytic deuteration using D_2O. *Nat. Commun.* **15**, 5231 (2024).
35. Hu, B. *et al.* Directing the C–N Coupling Pathway Enables Efficient Urea Electrosynthesis. *J. Am. Chem. Soc.* **147**, 21764-21777 (2025).
36. Wang, C. *et al.* Bimetallic $Cu_{11}Ag_3$ Nanotips for Ultrahigh Yield Rate of Nitrate-to-Ammonium. *Angew. Chem. Int. Ed.* **64**, e202415259 (2025).
37. Chen, L. *et al.* Engineering Gradient D-d Orbital Occupancy to Boost Substrate Adsorption for Efficient Electrocatalytic Biomass Valorization. *Angew. Chem. Int. Ed.* **64**, e202511868 (2025).
38. Yang, C., Zhang, L., Lu, Y., Zou, Y. & Wang, S. Designing efficient catalysts for electrocatalytic organic synthesis: From electronic structure to adsorption behavior. *Matter* **7**, 456-474 (2024).
39. Zhang, C. *et al.* Synergistic C–N Coupling for Efficient Cyclohexanone Oxime Synthesis from Ambient Air by Supported Molecular Catalysts. *Angew. Chem. Int. Ed.* **64**, e202506546 (2025).
40. Chen, T. *et al.* Functional Nanomaterials with Tip Effect: Synthesis and Applications in Electrocatalysis. *CCS Chem.* **0**, 1-23 (2025).
41. Liu, Y. *et al.* Embedded Fe-Cu Pairs Enable Tandem Nitrate-to-Ammonia Electroreduction. *Adv. Mater.* **38**, e14840 (2026).
42. Sun, L. *et al.* Enabling High Performance in a Positive Potential of Nitrate-to-Ammonia Electrocatalysis Over Mesoporous Core@Shell Cu_2O/Cu@PdCu Nanozyme. *Adv. Mater.* **37**, 2503291 (2025).
43. Zhu, L. *et al.* Alloyed Rhodium-Copper Nanocavities with Optimized Chemisorption of Hydrogen Radicals for Efficient Nitrate-to-Ammonia Electrocatalysis. *Small* **21**, 2502787 (2025).
44. Wu, Q., Fan, X., Liu, K., Quan, X. & Liu, Y. Efficient and selective electroreduction of nitrate to ammonia via interfacial engineering of B-doped Cu nanoneedles. *Appl. Catal. B Environ.* **361**, 124597 (2025).
45. Huang, Y., Gao, Y. & Zhang, B. Interfacial water regulation for water-participating electrocatalytic hydrogenation reactions. *Chem* **11** (2025).
46. Pan, F. *et al.* Long-Range Confinement-Driven Enrichment of Surface Oxygen-Relevant Species Promotes C–C Electrocoupling in CO2 Reduction. *Adv. Energy Mater.* **14**, 2303118 (2024).
47. Lan, J. *et al.* Isolating Cu-Zn active-sites in Ordered Intermetallics to Enhance Nitrite-to-Ammonia Electroreduction. *Nat. Commun.* **15**, 10173 (2024).
48. Sun, L., Yao, H., Wang, Y., Zheng, C. & Liu, B. Mesostructures Engineering to Promote Selective Nitrate-to-Ammonia Electroreduction. *Adv. Energy Mater.* **13**, 2303054 (2023).
49. Sun, L., Lv, H., Xiao, J. & Liu, B. Enzymatic Mesoporous Metal Nanocavities for Concurrent Electrocatalysis of Nitrate to Ammonia Coupled with Polyethylene Terephthalate Upcycling. *Adv. Mater.* **36**, 2402767 (2024).
50. Sun, L., Yao, H., Jia, F., Wang, Y. & Liu, B. Intermediate Confinement for Selective Ammonia Electrosynthesis from Nitrate on Robust Mesoporous Metal Catalysts. *Adv. Energy Mater.* **13**, 2302274 (2023).
51. Ma, Y. *et al.* Paddle-like self-stirring nanoreactors with multi-chambered mesoporous branches for enhanced dual-dynamic cascade reactions. *Nat. Nanotechnol.* **20**, 897-906 (2025).
52. Sun, L. & Liu, B. Microenvironment Engineering of Mesoporous Metals for Ammonia Electrosynthesis from Nitrate: Advances, Mechanisms, and Prospects. *Acc. Chem. Res.* **58**, 2306-2316 (2025).
53. Dai, Y. *et al.* Tandem Active Sites in Cu/Mo-WO_3 Electrocatalysts for Efficient Electrocatalytic Nitrate Reduction to Ammonia. *Adv. Funct. Mater.* **35**, 2420282 (2025).
54. He, H. *et al.* High-Entropy Effect of Mesoporous Metal Oxides Promotes Tandem Catalysis for Efficient Ammonia Electrosynthesis from Nitrate. *Adv. Mater.* **37**, e08982 (2025).
55. Li, Y. *et al.* The synergistic catalysis effect on electrochemical nitrate reduction at the dual-function active sites of the heterostructure. *Energy Environ. Sci.* **17**, 4582-4593 (2024).
56. Zuo, M. *et al.* In Situ Exsolution to Form Cu Nanoparticles on Cu–Doped $LaFeO_3$ Perovskite Oxides for Efficient Electrocatalytic Reduction of Nitrate to Ammonia. *Adv. Funct. Mater.* **36**, e13364 (2026).
57. Gu, X. *et al.* Tiara Ni Clusters for Electrocatalytic Nitrate Reduction to Ammonia with 97% Faradaic Efficiency. *J. Am. Chem. Soc.* **147**, 22785-22795 (2025).
58. Liu, J. *et al.* Elucidating the NH_2OH–Mediated Pathway for Photoelectrocatalytic C–N Coupling toward Solar-Driven Hexamethylenetetramine Synthesis. *J. Am. Chem. Soc.* **148**, 11779-11789 (2026).

59. Chen, X. *et al.* Amorphous Bismuth–Tin Oxide Nanosheets with Optimized C–N Coupling for Efficient Urea Synthesis. *J. Am. Chem. Soc.* **146**, 13527-13535 (2024).
60. Wang, N. *et al.* Tuning C–N Coupling Mode by Cu–In Dual Metal Sites in Covalent Organic Framework for Enhanced Urea Electrosynthesis. *Adv. Funct. Mater.* **35**, 2423683 (2025).
61. Tsigoias, S., Papanikolaou, M. G., Kabanos, T. A. & Kalampounias, A. G. Identification of Aggregation Processes in Hexamethylenetetramine Aqueous Solutions: A Comprehensive Raman and Acoustic Spectroscopic Study Combined with Density Functional Theory Calculations. *Molecules* **28**, 7838 (2023).
62. Dar, M. A., Kim, Y. S., Kim, W. B., Sohn, J. M. & Shin, H. S. Structural and magnetic properties of CuO nanoneedles synthesized by hydrothermal method. *Appl. Surf. Sci.* **254**, 7477-7481 (2008).
63. Liu, J. *et al.* Mesoporous Cu_2O submicro-spheres, facile synthesis and the selective adsorption properties. *Chem. Eng. J.* **185-186**, 151-159 (2012).

Acknowledgements

The authors would like to thank Dr. Feng Yang (the Comprehensive Training Platform of the Specialized Laboratory, College of Chemistry, Sichuan University) for her assistance with TEM/STEM imaging, Dr. Yanhong Liu (the Comprehensive Training Platform of the Specialized Laboratory, College of Chemistry, Sichuan University) for her assistance of Raman tests, and Dr. Yanping Huang (the Center of Engineering Experimental Teaching, School of Chemical Engineering, Sichuan University) for her help of SEM imaging.

Funding

This work was financially supported by the National Natural Science Foundation of China (22575159, B.L. and 22505167, L.S.), the China National Postdoctoral Program for Innovative Talents (BX20250117, L.S.), the China Postdoctoral Science Foundation (2025M781000, L.S.), and the Fundamental Research Funds for the Central Universities (B.L.).

Author contributions

L.S. and Y.J. conducted the experiments, performed the structural characterizations and calculations, and analyzed the data. B.L. conceived and supervised the project. All the authors discussed the results and cowrote the paper.

Competing interests

The authors declare no conflict of interest.

Figure Legends/Captions

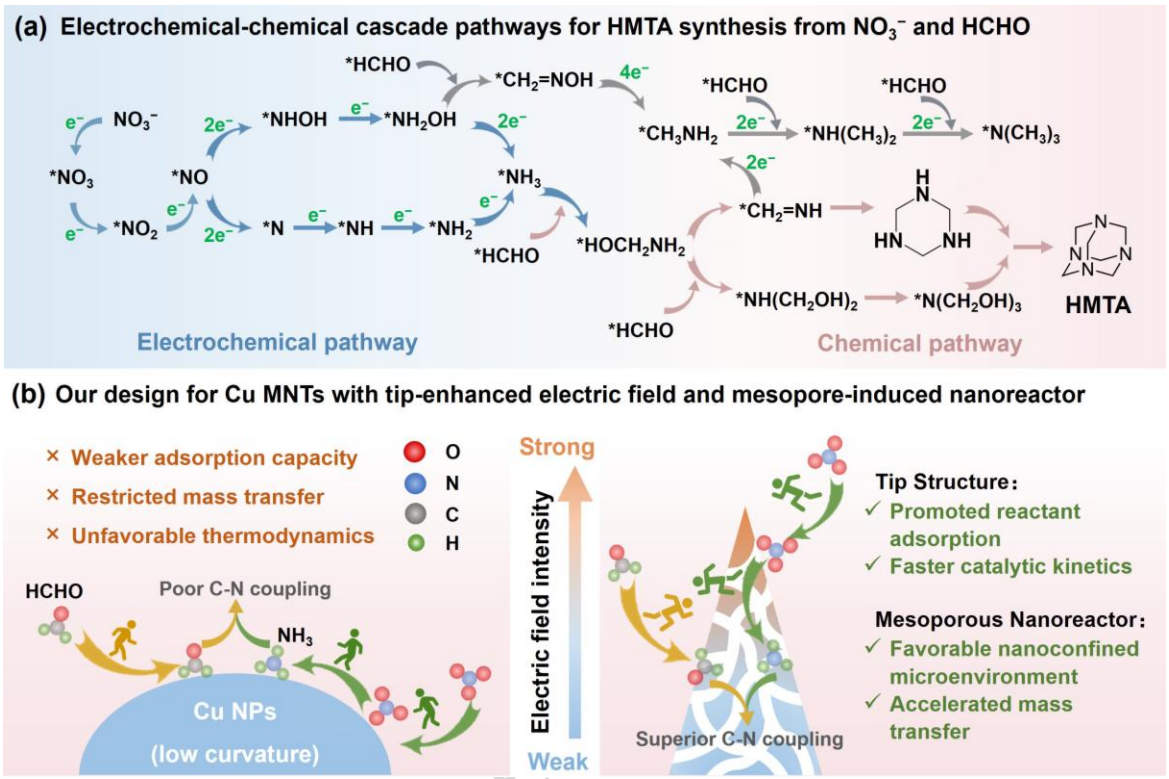

Figure 1. **Reaction pathways and catalyst design strategy for HMYA synthesis from NO_3^- and HCHO.** (a) Synthetic pathways of high-value HMTA from NO_3^- and HCHO. (b) Designed principle of Cu MNTs with synergistically tip-enhanced electric field and mesopore-induced nanoreactor for selective HMTA synthesis.

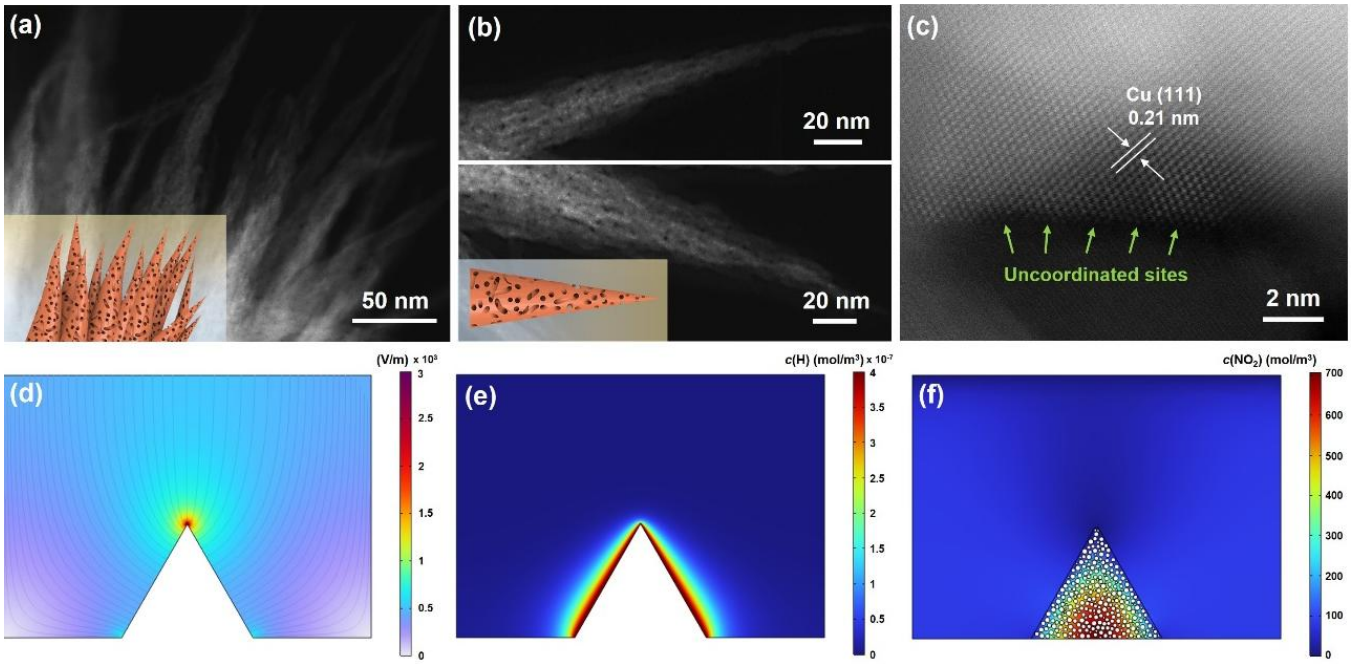

Figure 2. Catalyst characterizations and chemisorption properties. (a) Low-magnification and (b) high-magnification HAADF-STEM images, and (c) high-resolution HAADF-STEM image of Cu MNTs. Insets in (a, b) are schematic models of Cu MNTs. (d) Local electric field around the NTs. (e) FEM simulated concentrations and distributions of active hydrogen on NTs. (f) FEM simulated concentrations and distributions of NO_2^- on MNTs.

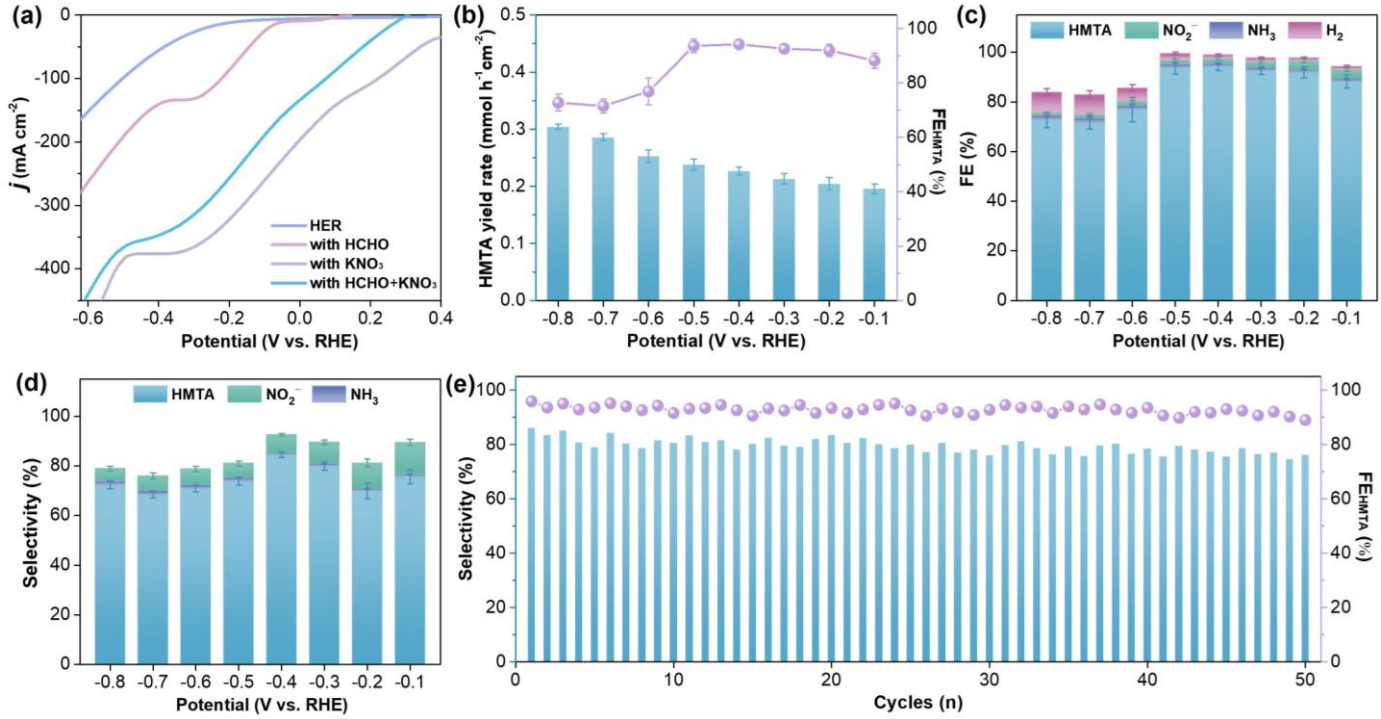

Figure 3. Catalytic performance of Cu MNTs for HMTA synthesis. (a) LSV curves of Cu MNTs collected in different electrolytes (Potentials are non-*i*R-corrected). (b) HMTA yield rate and FE_{HMTA} value of Cu MNTs collected in different applied potentials. (c) FE_{HMTA} and (d) HMTA selectivity of Cu MNTs for different products in different applied potentials. (e) Consecutive recycling tests of Cu MNTs for reaching 50 cycles. Error bars denote the standard deviations calculated from three independent measurements. Experimental conditions: electrocatalytic reaction was conducted in an H-cell separated by a Nafion 117 membrane under ambient conditions (room temperature (25 ± 2 °C)). Catalyst loading: 2.0 mg cm^{-2} on carbon paper (1.0 × 1.0 cm^2). Electrolyte: 30 mL of 0.10 M KOH + 0.50 M K_2SO_4 + 0.10 M KNO_3 + 0.30 M HCHO (pH = 13 ± 0.2). Scan rate: 10 mV s^{-1}. The catholyte was continuously stirred at 300 rpm. All the electrochemical performance tests were without *iR* compensation. Source data for Figure 3 are provided as a Source Data file.

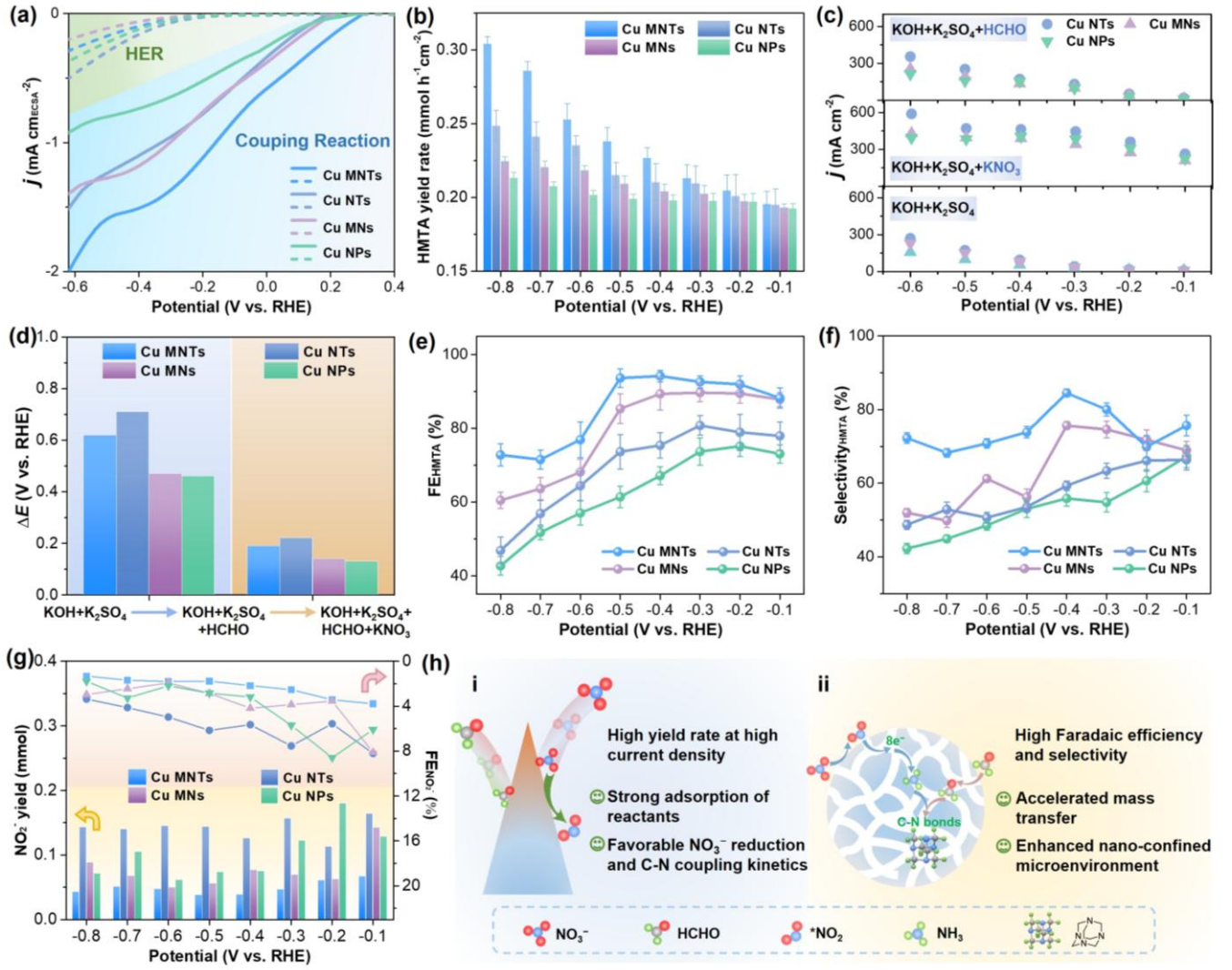

Figure 4. Mechanism exploration of electrochemical and chemical cascade catalysis for C–N coupling reaction. (a) Normalized LSV curves of Cu MNTs, Cu NTs, Cu MNs, and Cu NPs collected in 0.10 M KOH and 0.50 M K_2SO_4 with and without 0.30 M HCHO and 0.10 M KNO_3. (b) HMTA yield rates of Cu MNTs, Cu NTs, Cu MNs, and Cu NPs collected in different applied potentials. (c) Total current densities of Cu NTs, Cu MNs, and Cu NPs collected in different applied potentials. (d) OCP changes of Cu MNTs, Cu NTs, Cu MNs, and Cu NPs collected in 0.10 M KOH and 0.50 M K_2SO_4 with and without 0.30 M HCHO or 0.10 M KNO_3. (e) FE_{HMTA} values and (f) HMTA selectivity of Cu MNTs, Cu NTs, Cu MNs, and Cu NPs collected in different applied potentials. (g) NO_2^- yield and FE_{NO2-} values of Cu MNTs, Cu NTs, Cu MNs, and Cu NPs collected in different applied potentials. (h) Schematic illustration of performance enhancement for HMTA synthesis by synergistic (i) tip-enhanced local electric field effect and (ii) mesopore-induced confinement effect. Error bars denote the standard deviations calculated from three independent

measurements. All the electrochemical performance tests were without *iR* compensation. Source data for Figuer 4 are provided as a Source Data file.

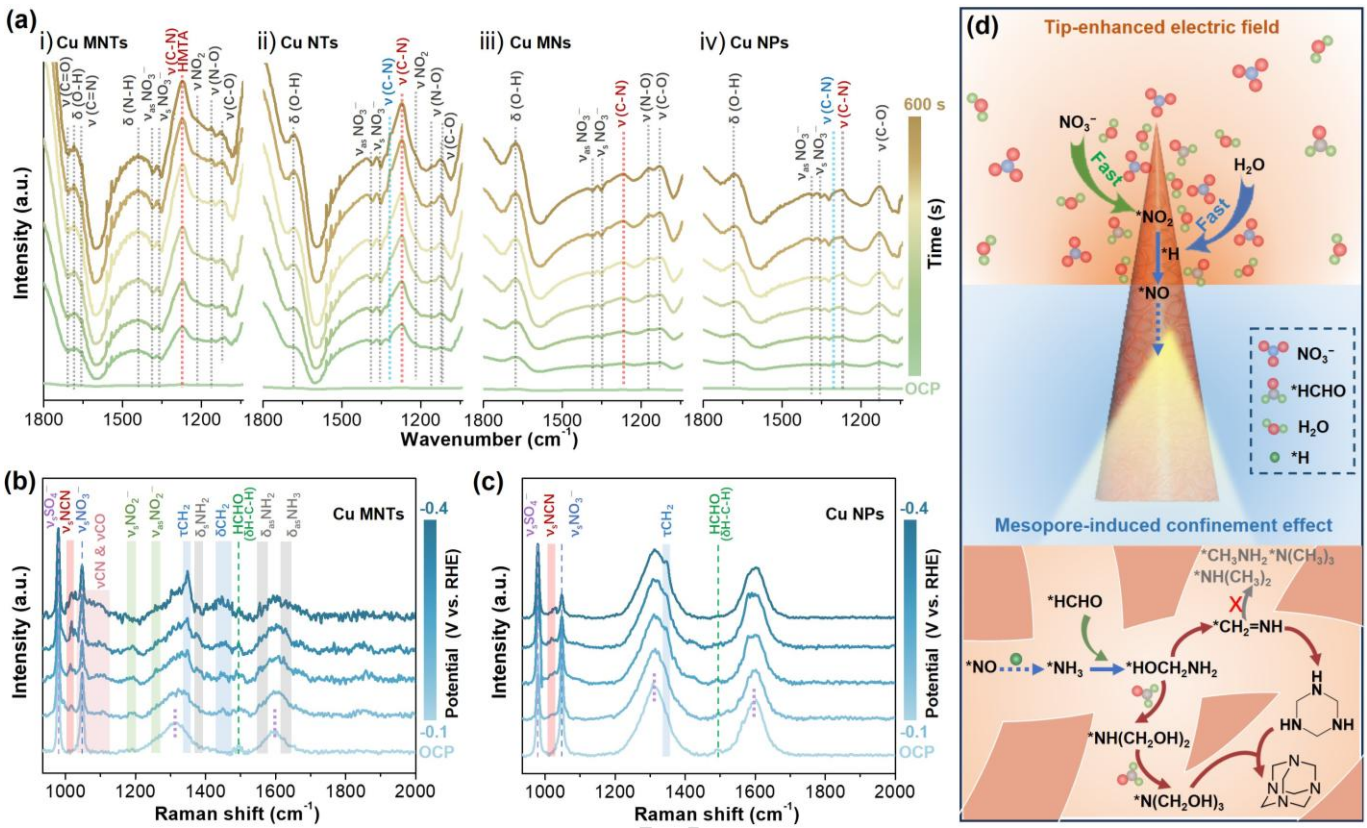

Figure 5. *In situ* electrochemical spectroscopy studies. (a) *In situ* FTIR spectra of Cu MNTs, Cu NTs, Cu MNs, and Cu NPs collected in different test times. *In situ* Raman spectra of (b) Cu MNTs and (c) Cu NPs collected in different applied potentials. (d) Proposed electrochemical-chemical cascade pathways and mechanism of Cu MNTs for selective HMTA synthesis from NO_3^- and HCHO. All the electrochemical performance tests were without *iR* compensation. Source data for Figure 5 are provided as a Source Data file.

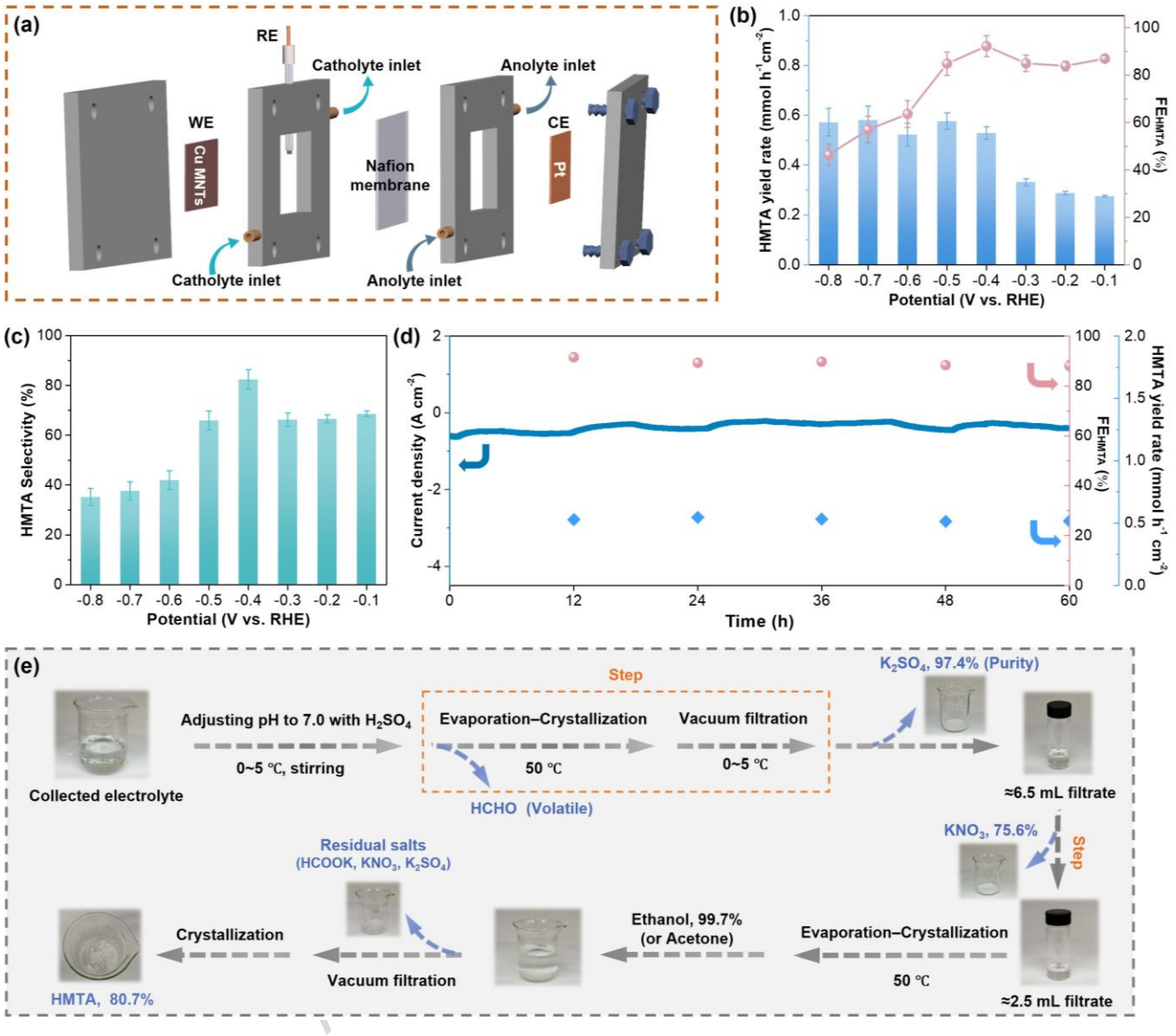

Figure 6. Product separation and economic analysis. (a) Schematic illustration of flow cell reactor for HMTA synthesis with Cu MNTs as catalyst. (b) HMTA yield rate and FE_{HMTA} value, (c) HMTA selectivity, and (d) stability collected in 0.10 M KOH and 0.50 M K_2SO_4 containing 1.50 M HCHO and 0.50 M KNO_3 in flow reactor. (e) Schematic illustration of real-world HMTA synthesis and purification process. Error bars denote the standard deviations calculated from three independent measurements. All the electrochemical performance tests were without *iR* compensation. Source data for Figure 6 are provided as a Source Data file.

Editor's Summary:

Electrochemical-chemical cascade synthesis of hexamethylenetetramine is promising yet challenged by low selectivity and yield. Here, the authors report copper catalysts of hierarchical tip and mesopore where tip-enhanced effect and nanoreactor confinement synergistically boost selectivity and yield.

Peer review information: *Nature Communications* thanks Mufan Li and the other anonymous reviewer(s) for their contribution to the peer review of this work. A peer review file is available.